

## Engineering Protein-Based Lipid-Binding Nanovesicles via Catechol-Amine-Derived Coacervation with Their Underlying Interfacial Mechanisms

Haibing Yang,<sup>||</sup> Yao Song,<sup>||</sup> Qiang Zhang, Moran Wang, Tianqi Jia, Qing Pan,<sup>\*</sup> Kanda Sun, Xiang Guan, Mingfei Pan, Feng Chen,<sup>\*</sup> and Bin Yan<sup>\*</sup>



Cite This: *Langmuir* 2025, 41, 3199–3208



Read Online

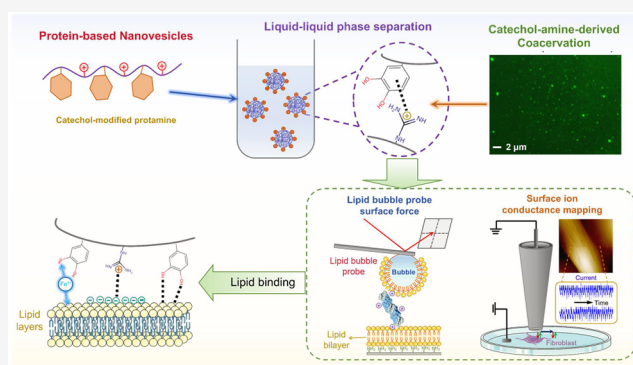
ACCESS |

Metrics & More

Article Recommendations

Supporting Information

**ABSTRACT:** The development of nonphospholipid nanovesicles has garnered tremendous attention as a viable alternative to traditional liposomal nanovesicles. Protein/peptide-based nanovesicles have demonstrated their potential to reduce immunogenicity while enhancing bioactivity. However, a fundamental understanding of how proteinaceous vesicles interact with lipids and cell membranes remains elusive. In this study, we engineered a series of protamine-based nonphospholipid nanovesicles by modulating intramolecular catechol–amine interactions. By grafting trihydroxybenzene (GA) and catechol (CA) groups onto the protamine (Prot), a salt-triggered coacervation was observed in an alkaline environment with the size of as-prepared vesicles ranging from 200 to 1200 nm. The bonding affinity to lipid interfaces followed the order of Prot-CA-Fe<sup>3+</sup> (25  $\mu$ M) > Prot-CA-Fe<sup>3+</sup> (10  $\mu$ M) > Prot-CA > original Prot with the underlying nanomechanics investigated by the lipid bubble force measurement. Direct quantification of interactions between the nanovesicles and living human gingival fibroblasts was performed by using surface charge difference mapping. Introducing trace amounts of Fe<sup>3+</sup> (at 10 and 25  $\mu$ M) enhanced vesicle–lipid interactions via the synergy of catechol–amine interactions and Fe<sup>3+</sup>-induced complexation. This work provides improved valuable insights into the interactions between nanovesicles and cell membranes, offering an energetic paradigm for modulating cell-target delivery processes via intramolecular short-range interactions.



### INTRODUCTION

The innovation of nanovesicles for modern medicine has significantly improved the therapeutic efficacy of drugs, exosomes, and cells.<sup>1–3</sup> Traditional phospholipid-based nanovesicles demonstrate their strengths in encapsulating therapeutic agents with enhanced biocompatibility, physiological solubility, and deep tissue permeability.<sup>4–6</sup> Meanwhile, the core–shell structure of phospholipid-based nanovesicles also provides the controlled and sustained release of drugs, while preventing the undesirable degradation of certain medications upon exposure to enzymes. However, the loading capacity of phospholipid-based nanovesicles is limited by their hydrophobic core, and their hydrophilic shell typically hinders active transport across the cell membrane.<sup>7,8</sup> In light of these drawbacks, nonphospholipid nanovesicles have been developed to complement the existing liposomal delivery system.<sup>9–11</sup> Cell-penetrating proteins/peptides for transporting macromolecules (e.g., nucleic acids, proteins, and drugs) are thus investigated for fine-tuning cellular functions and therapeutic applications.<sup>12,13</sup> However, the process of macromolecules penetrating cell membranes is complicated, governed by protein–protein and protein–lipid interactions between the

nanovesicles and cell membranes. A profound understanding of these transportation mechanisms is still lacking, which restricts the reliable application of protein/peptide-based nonphospholipid nanovesicles.

Previous research has identified several protein/peptide-based cell-penetration phenomena, including endocytosis, membrane perforation, and helical structure-induced membrane penetration.<sup>14</sup> Among all of these reported cell-penetrating proteins and peptides, protamine has garnered significant attention due to its stable encapsulation capabilities and universal binding properties to lipids.<sup>15</sup> Protamine is a class of polycationic arginine-rich peptides found in the sperm of salmon and scombridae, with molecular weights ranging from 4000 to 5000 Da (short proteins).<sup>16</sup> Within the sperm,

**Received:** October 7, 2024

**Revised:** January 24, 2025

**Accepted:** January 26, 2025

**Published:** February 2, 2025



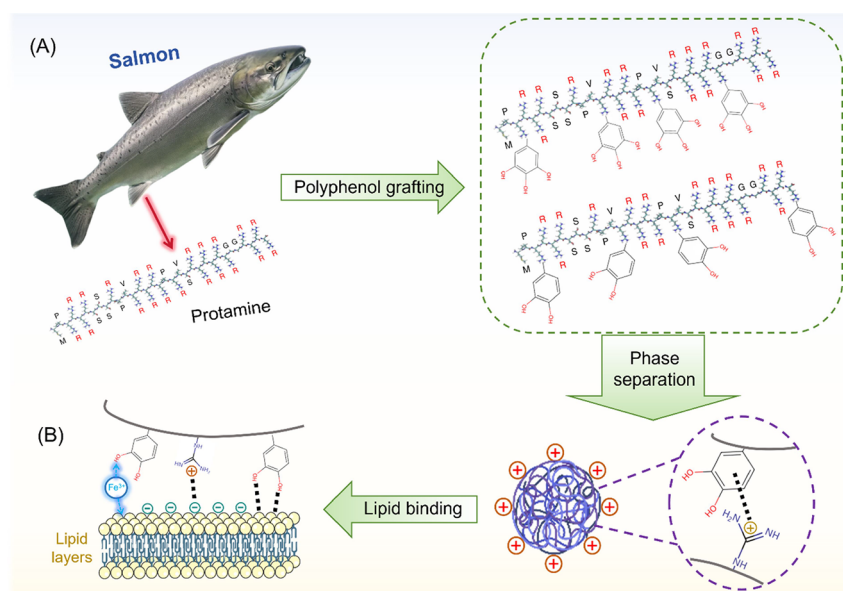


**Figure 1.** Design of protamine-based nonphospholipid nanovesicles. (A) Schematic illustration of protamine derived from salmon sperm and the polyphenol grafting of GA and CA. (B) Demonstration of catechol–amine interaction-induced phase separation and the interfacial interaction mechanisms of enhanced lipid binding of Prot-CA-Fe<sup>3+</sup>.

cationic protamine serves as a cargo molecule to densely package anionic DNA by electrostatic linkage-derived protein–nucleic acid condensation, thereby protecting DNA from enzymatic degradation and UV radiation.<sup>17</sup> Although protamine has been reported to significantly enhance the cellular uptake of therapeutic agents, such as miRNA and drugs, the delivery efficiency of single protamine as the cargo molecule in complex physiological environments remains suboptimal.

Herein, inspired by the complex coacervation behavior of mussel foot proteins with adjacent catechols and amines that account for >50 mol % of their amino acid side chains,<sup>18,19</sup> we engineer a series of protamine-based nonphospholipid nanovesicles by refining the intramolecular catechol–amine interactions. By grafting trihydroxybenzene (GA) and catechol (CA) groups onto protamine (Prot), a spontaneous phase separation phenomenon was observed in an alkaline environment, resulting in vesicles of varying sizes from 200 to 1200 nm (Figure 1A). The atomic force microscopy (AFM) bubble probe technique was employed to directly quantify the surface forces between lipid-stabilized bubbles and Prot and Prot-CA in a mildly alkaline environment.<sup>20</sup> Meanwhile, the influence of Fe<sup>3+</sup> at low concentrations of 10 and 25 μM on the protein–lipid interactions was further investigated. The binding affinity of Prot-CA-Fe<sup>3+</sup> to lipid membranes was modulated by the synergy of catechol–amine interactions and Fe<sup>3+</sup>-induced complexation (Figure 1B), as investigated by scanning ion conductance mapping (SICM) on living human gingival fibroblasts (HGFs), complemented by antibacterial assays against *E. coli* and *S. aureus*. Owing to the precise molecular design, it was hypothesized that the binding affinity of as-prepared Prot-CA to the cell membrane was significantly enhanced, which holds great promise to be further engineered and utilized as nonphospholipid nanovesicles for drug delivery within clinical procedures.

## METHODS

**Chemicals and Materials.** Protamine (sulfate salt from salmon, Sigma-Aldrich, US), gallic acid (GA; Sigma-Aldrich, US), caffeic acid

(CA; Sigma-Aldrich, US), *N*-(3-(dimethylamino)propyl)-*N'*-ethylcarbodiimide hydrochloride (EDC, Sigma-Aldrich, US), *N*-hydroxysuccinimide (NHS, Sigma-Aldrich, US), 1,2-dioleoyl-*sn*-glycero-3-phosphoethanolamine (>99%, Sigma-Aldrich, US), 2-morpholinoethanesulfonic acid (MES, Sigma-Aldrich, US), and phosphate-buffered saline (PBS, pH = 7.4, Sigma-Aldrich, US) were purchased from Sigma-Aldrich (CN). Deionized (DI) water, obtained from the Barnstead Smart2Pure pro water purification system (Thermo Fisher Scientific, CN), was utilized in all experiments conducted in this study.

**Synthesis of Prot-GA and Prot-CA via EDC/NHS Grafting.** A 4 mg/mL portion of Prot was first dissolved in 0.2 M MES buffer (pH 6.5) under stirring at room temperature followed by the addition of 1.5 mg/mL GA or CA until a clear solution was obtained. After that, 0.5 mg/mL EDC and 0.5 mg/mL NHS were introduced into the mixture solution to enable the amide grafting of GA/CA to the amine groups of Prot. After a 6 h reaction period, the mixture was dialyzed to obtain the final products Prot-GA and Prot-CA.

**Surface Modifications of PDMS Substrates.** Surface modifications of commercial polydimethylsiloxane (PDMS, Suzhou Jiutao Sensing Technology) substrates were performed as previously reported.<sup>49</sup> In brief, the PDMS substrates were subjected to oxygen plasma for 5 min in a plasma cleaner (Harrick Plasma-PDC 002) followed by immersion in a 5% 3-aminopropyltriethoxysilane (APTES) solution at room temperature for 1 h. The APTES-modified PDMS was treated with 0.5% glutaraldehyde (Glu) for 1 h and 5% bovine serum albumin (BSA) for 3h, rinsed with deionized water, and then allowed to dry in air.

**Characterization of the Samples.** Dynamic light scattering (DLS), UV–vis spectroscopy, X-ray photoelectron spectroscopy (XPS), and scanning electron microscopy (SEM) were performed to characterize the developed materials. The hydrodynamic diameters of Prot-GA and Prot-CA were characterized by DLS (Litesizer DLS 500, Anton Paar). The transmittance of the samples at various concentrations was assessed by UV–vis spectroscopy (Cary 4000, Agilent Technologies) at a wavelength of 600 nm. The chemical composition of the as-prepared coatings was analyzed by UV–vis spectroscopy and XPS. Prot, Prot-GA, and Prot-CA were deposited onto polyvinyl chloride (PVC) wafers at a concentration of 2 mg/mL. Prior to SEM characterization, a thin layer of gold (~14 nm) was sputtered on the coated PVC wafers. The surface morphologies of Prot, Prot-GA, and Prot-CA on PVC wafers were examined by field-

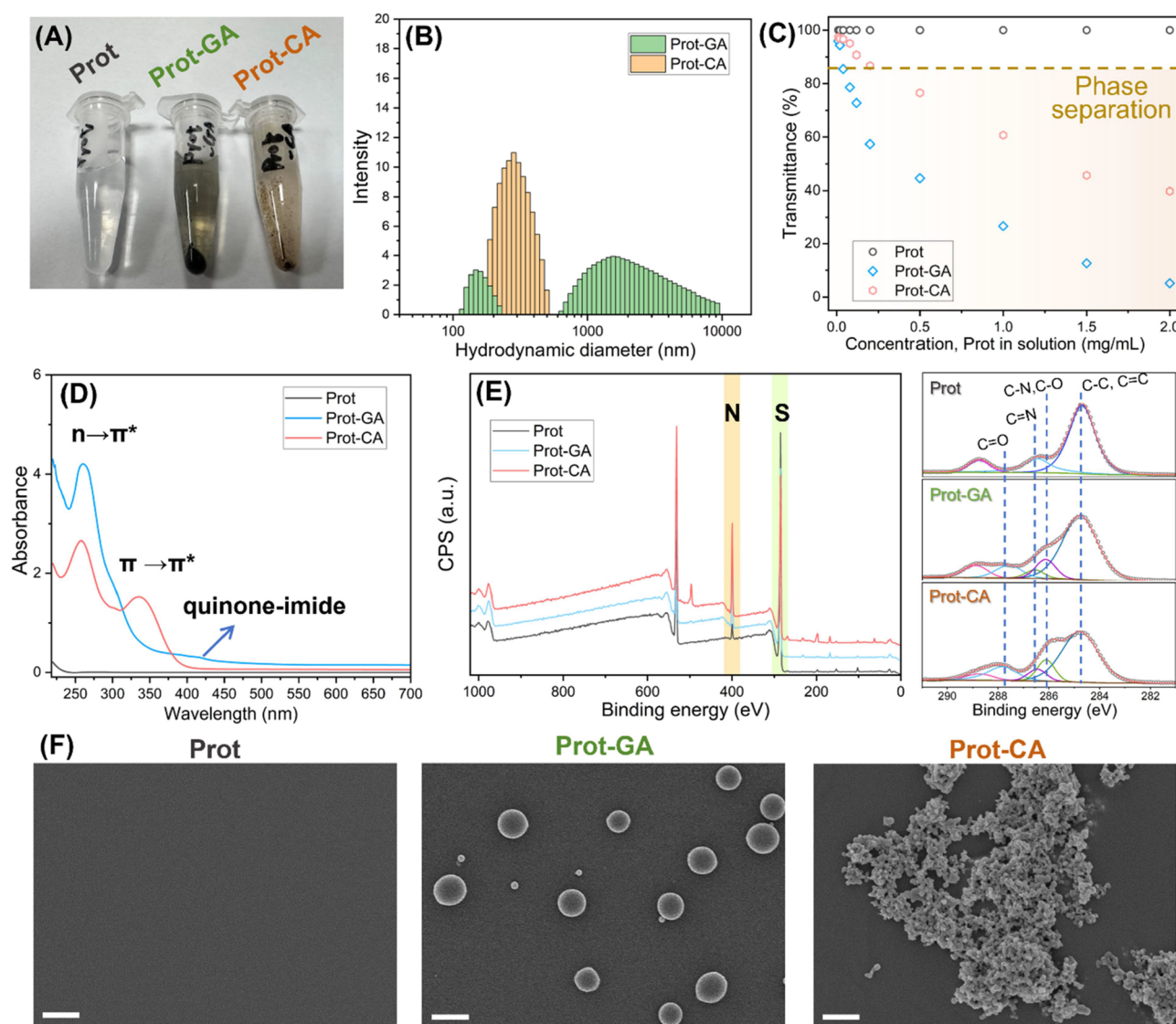


**Figure 2.** (A) Optical images of Prot, Prot-GA, and Prot-CA at a concentration of 1 mg/mL in PBS following centrifugation. (B) DLS analysis of Prot-GA and Prot-CA in PBS solution. (C) Transmittance measurements of Prot, Prot-GA, and Prot-CA across a concentration range of 0.01–2 mg/mL (Prot in solution), characterized by their UV–vis spectra. (D) UV–vis spectra of Prot, Prot-GA, and Prot-CA within the wavelength range of 220–700 nm. (E) XPS wide-scan spectra of Prot, Prot-GA, and Prot-CA deposited on PVC wafers, along with the corresponding high-resolution C deconvolution spectra. (F) SEM images of bare Prot, Prot-GA, and Prot-CA coatings on PVC wafers, captured at a magnification of 10k (scale bar = 2  $\mu$ m).

emission SEM (FE-SEM, Zeiss Sigma 300 VP-FESEM, Germany), at an acceleration voltage of 10 keV.

**Nanopipette Preparation.** Borosilicate microglass capillaries were utilized and processed through a P-2000G laser-pulling device to fabricate the microelectrode probes. The parameters for this procedure were set to HEAT = 275, FIL = 4, VEL = 50, DEL = 225, and PUL = 150, resulting in a probe tip with an inner diameter of approximately 70 nm.

**Surface Potential and Charge Characterization of the Samples.** Zeta potential measurements (Litesizer DLS 500, Anton Paar) were conducted to evaluate the overall surface charges of Prot, Prot-GA, and Prot-CA in a diluted saline solution (10 mM NaCl) while varying the solution pH. The topographical and  $\Delta I$  images of the BSA, Prot-GA, and Prot-CA coating on PDMS substrates were obtained by XE-Bio SICM in approach-retract scan (ARS) and skip modes, as reported previously. BSA, Prot-GA, and Prot-CA were deposited on PDMS substrates via dip-coating methods with a mass concentration of 0.5 mg/mL in PBS buffer. Briefly, the SICM system first conducts a coarse scan (typically with 64 or 32 points) to assess the overall height variation, followed by a fine scan (typically with 256

or 128 points). Initially, the nanopipette approached the sample from its starting position ( $D_{ps-max}$ ). Once the ionic current dropped to a predetermined threshold, the probe was halted at the minimum distance position ( $D_{ps-min}$ ). The probe was then retracted back to  $D_{ps-max}$  with a digital oscilloscope recording the probe's position and ionic current signals. By evaluating the ionic current, the  $\Delta I$ -SICM images were reconstructed based on the repeated fine approaches of the probe, reflecting the variations in surface charge.

**Force Measurement Using the Bubble Probe AFM Technique.** The interaction forces between bubbles adsorbed with dioleoylphosphatidylethanolamine (DOPE) adsorbed at the interface and DOPE-coated mica surfaces in NaCl solutions were directly measured by the AFM bubble probe technique on an MPF-3D AFM (Asylum Research, Santa Barbara, CA, USA). The detailed experimental procedures were reported previously by our group. The mica surface was first treated with APTES followed by a lipid-transfer process in PBS to enable a DOPE double layer deposition on the mica surfaces. For bubble probe preparation, bubbles were generated by squeezing methods from an ultrasharp glass micropipette into the saline containing 200 ppm of DOPE on a glass



substrate of the AFM fluid cell. Then, bubbles on the fluid cell would remain for 20 min until the equilibrium of the air/water interface with the surfactant in saline solution. Subsequently, a bubble with the appropriate size (radius  $\sim 50$ – $100\ \mu\text{m}$ ) was carefully picked up by an AFM tipless rectangular cantilever with a circular gold patch on the end, which had been hydrophobized by immersion in 10 mM dodecanethiol in ethanol solution overnight. Finally, the bubble-anchored cantilever (bubble probe) was maneuvered and positioned over the DOPE-coated mica substrate in the fluid cell for force measurements. The spring constant of the AFM cantilever was calibrated to be 0.3–0.4 N/m using the Hutter and Bechhoefer thermal tune method. During force measurements, the drop probe was driven to approach the silicon substrate at a fixed velocity until a preset deflection ( $\sim 10\ \text{nN}$ ) was detected, at which point it was retracted from the surface. The interaction force was calculated based on the spring constant and the deflection of the cantilever by Hooke's Law.

**Cell Culture and Mapping.** HGFs were cultured in DMEM (HyClone, Logan, USA), supplemented with 1% penicillin, 1% streptomycin (HyClone, Logan, MA, USA), and 10% fetal bovine serum (Gibco, California, USA). The cells were incubated in a humidified chamber at  $37\ ^\circ\text{C}$  in a 5%  $\text{CO}_2$  atmosphere. To minimize ionic current fluctuations and reduce cell damage during scanning, the cells were grown on soft PDMS films. Prior to cell seeding, the PDMS films were treated with 0.1% gelatin and fibronectin to enhance the surface cytoaffinity and promote cell adhesion. After a 24 h seeding period, cell adhesion was assessed, and the culture medium was replaced to ensure optimal growth conditions. The samples were washed three times with PBS to remove the debris and residues. During detection, DMEM was added to maintain the cell vitality and physiological conditions. A dual-mode approach, specifically ARS and skip, was employed to capture both morphological and  $\Delta I$  images.

**Antibacterial Activity Assay.** Antibacterial experiments of group 1 (control), group 2 (Prot-CA), group 3 (Prot-CA- $\text{Fe}^{3+}$  (10  $\mu\text{M}$ )), and group 4 (Prot-CA- $\text{Fe}^{3+}$  (25  $\mu\text{M}$ )) were conducted by the spread plate method. Gram-negative *E. coli* (ATCC25922) and Gram-positive *S. aureus* (ATCC25923) were utilized as the model microbials for investigation. In a typical spread plate procedure, group 2 (Prot-CA-0.2 mg/mL), group 3 (Prot-CA-0.2 mg/mL- $\text{Fe}^{3+}$  (10  $\mu\text{M}$ )), and group 4 (Prot-CA-0.2 mg/mL- $\text{Fe}^{3+}$  (25  $\mu\text{M}$ )) were incubated with 1 mL of *E. coli* in Luria–Bertani (LB) nutrient solution at  $10^6$  CFU/mL in a 12-well plate at  $37\ ^\circ\text{C}$ , followed by mild shaking for 4 h. The suspension was then evenly spread on LB agar plates and incubated at  $37\ ^\circ\text{C}$  for 12 h. Colonies on each plate were counted by ImageJ software, and the inhibition rates of groups 2–4 were calculated according to the number of colonies of the group compared with that of the control groups.

**Statistical Analysis.** Averages and standard deviations (SDs) were calculated from at least three independents for each data entry. The data were processed with Excel (version 2405) and classified according to the  $p$  values ( $t$ -test, two-sided) and denoted by (ns) for  $p > 0.05$ , (\*) for  $p < 0.05$ , (\*\*) for  $p < 0.01$ , (\*\*\*) for  $p < 0.001$ , and (\*\*\*\*) for  $p < 0.0001$ .

## RESULTS AND DISCUSSION

**Syntheses of Prot-GA and Prot-CA.** Due to the highly efficient protective functions of protamine found in the sperm of salmon and scombridae, the polycationic arginine-rich backbones were investigated and further engineered in this work. Short-range interactions between adjacent catechols and amines have been reported to promote self-coacervation, driven primarily by inter- and intramolecular catechol–amine interactions, inspired by the mussel foot protein (Mfp-3 and Mfp-5).<sup>21–23</sup> A strategy for developing nonphospholipid nanovesicles was adopted in this work. The pristine protamine (Prot) was modified through grafting with GA and CA in a solution containing 1-ethyl-3-(3-dimethyl aminopropyl) carbodiimide hydrochloride/*N*-hydroxysulfosuccinimide

(EDC-NHS, pH = 6.5).<sup>24</sup> The process formed amide bonds between the carboxyl groups of GA and CA and the amine group of Prot. Following the grafting procedure, the products were dialyzed to remove the unreacted components and diluted in a PBS solution (pH = 7.4). Figure 2A illustrates the optical images of the obtained Prot-GA and Prot-CA, revealing that Prot-CA exhibited less protein–phenol condensation compared to Prot-GA after centrifugation at room temperature ( $\sim 25\ ^\circ\text{C}$ ). The hydrodynamic diameters of Prot-GA and Prot-CA were characterized using DLS (Figure 2B), showing peaks at 282 and 1681 nm, respectively. This confirmed the self-assembly of Prot-GA and Prot-CA into nanosized droplets through phase separation, with a secondary peak observed at 160 nm for Prot-GA.<sup>25,26</sup> The effect of concentration on the phase separation was thus investigated by the UV–vis spectrum. The transmittance at 600 nm decreased as the concentration increased from 0.01 to 2 mg/mL (the concentration of Prot in solution), with a significant decrease in transmittance for Prot-GA over 0.04 mg/mL and Prot-CA over 0.2 mg/mL (Figure 2C). Notably, Prot-CA formed relatively smaller vesicles compared to Prot-GA at the same mass concentration. The UV–vis and XPS spectra were obtained to characterize the chemical functionality of the developed Prot-GA and Prot-CA. Compared to the UV–vis spectrum of the original Prot, the peaks located at 280 and 335 nm (Figure 2D) correspond to the  $n \rightarrow \pi^*$  and  $\pi \rightarrow \pi^*$  electronic transitions of  $-\text{C}=\text{O}$  and aromatic moieties of Prot-GA and Prot-CA, while the peaks located at 420 nm correspond to quinone–imide compounds of Prot-GA.<sup>27–29</sup> To further elucidate the contribution of catechol–amine interactions to coacervation, XPS scans of the full spectrum and detailed C and N spectra were recorded (Figure 2E). The detailed C 1s and N 1s spectra are presented in Figures 2E and S1, respectively. These deconvoluted spectra included a C–C/C=C peak with a binding energy of  $\sim 284.8\ \text{eV}$ , a C–N/C–O peak with a binding energy of  $\sim 286\ \text{eV}$ , a C=N peak with a binding energy of  $\sim 286.8\ \text{eV}$ , a C=O (carbonyl group) peak with a binding energy of  $\sim 287.8\ \text{eV}$ , and an O–C=O (carboxylate group) peak with a binding energy of  $\sim 288.8\ \text{eV}$ .<sup>30,31</sup> Moreover, the presence of the C–N/C–O peak confirmed the successful grafting of GA and CA onto the Prot scaffold. These results indicate that catechol and trihydroxybenzene groups play important roles in the phase separation process of Prot.

**Characterization of Prot-GA and Prot-CA.** We then applied the developed Prot-GA and Prot-CA on the PVC wafer as the coating materials. The morphologies of the deposited Prot, Prot-GA, and Prot-CA at a mass concentration of 2 mg/mL were characterized by FE-SEM, as shown in Figures 2F and S2 (higher magnification). In comparison to the uniform coating of Prot on the PVC wafer, Prot-GA exhibited a nonporous spherical shape with diameters exceeding  $1\ \mu\text{m}$  in the dry state, while Prot-CA exhibited significant aggregation assembled by smaller spheres of approximately 200 nm in size. The morphologies of Prot-GA and Prot-CA in the dry state were consistent with their hydrated state, as corroborated by fluorescent images in Figure S3. We investigated the entrapment efficiency using Rhodamine 6G (R-6G) as the model drug molecule, characterized by UV–vis spectra (Figure S4A). As shown in Figure S4B of the revised Supporting Information, the original R-6G solution and the supernatant of R-6G/Prot-CA solution after centrifugation at room temperature ( $\sim 25\ ^\circ\text{C}$ ) were used to calculate the entrapment



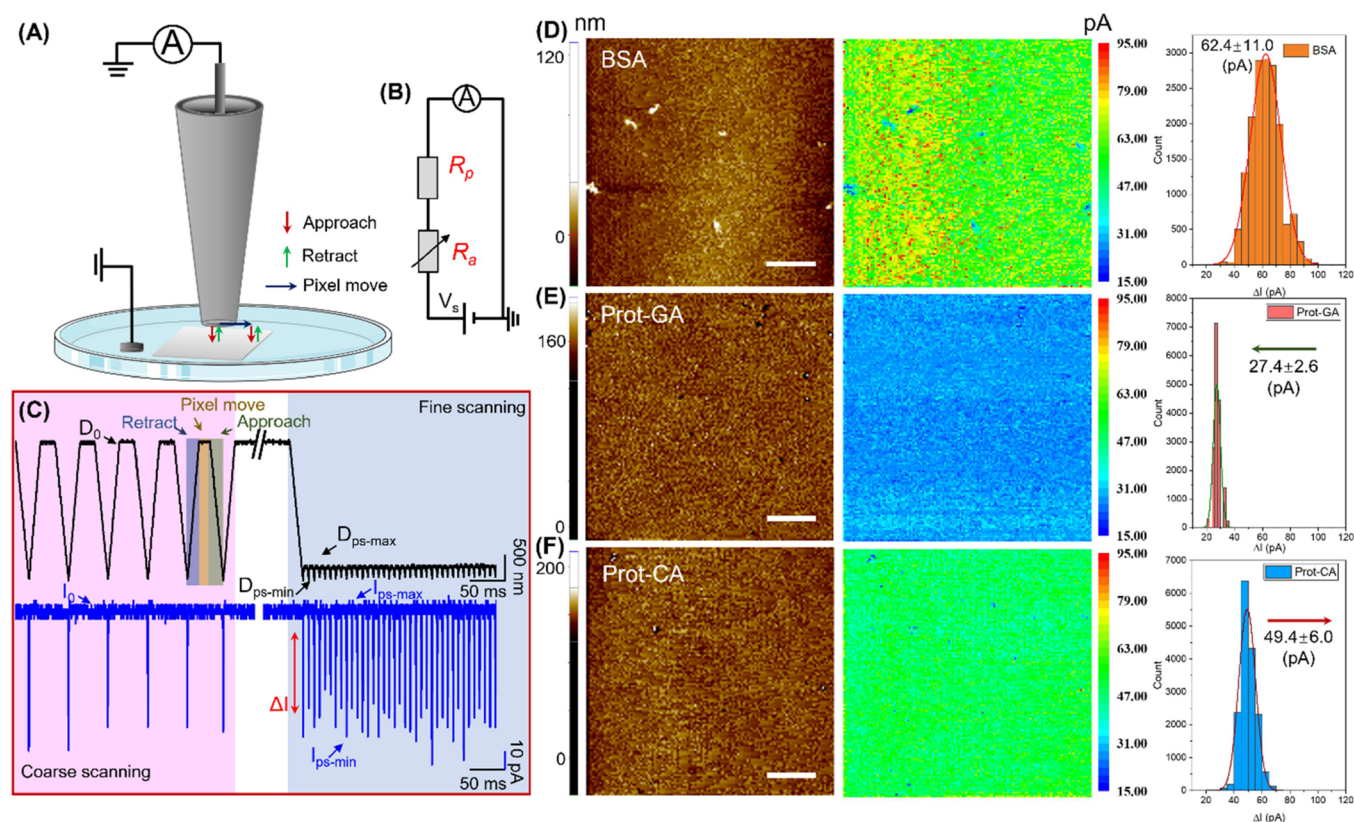


**Figure 3.** Surface charges of the developed nanovesicles. (A) Schematic of the  $\Delta I$ -based SICM configuration with a borosilicate glass nanopipette as a probe. (B) The equivalent circuit for ionic current measurement using sample bias mode. (C) Time traces of Z movement (black) and ionic current (blue), with blue, yellow, and green shaded regions indicating approach, retract, and pixel movement, respectively. Topographical maps (left column),  $\Delta I$  images (middle column), and  $\Delta I$  histograms (right column) of the BSA (D), Prot-GA (E), and Prot-CA (F)-coated PDMS substrates in PBS by using the  $\Delta I$ -based SICM (scale bar, 1  $\mu\text{m}$ ).

efficiency of Prot-CA. A passive encapsulation of R-6G to Prot-CA during the phase separation process was observed, and the entrapment efficiency was around 50% with the concentration of R-6G ranging from 6 to 20  $\mu\text{g/mL}$ . The surface potential and charge differences of the developed Prot-GA and Prot-CA were assessed by zeta potential analysis and SICM. As indicated in Figure S5, the zeta potentials of these proteins followed the order Prot > Prot-GA > Prot-CA across a pH range of 4–10, demonstrating the influence of the negatively charged GA and CA moieties mediating their interfacial charges. Meanwhile, the zeta potentials of Prot-CA were relatively close to the isoelectric point compared to that of Prot-GA, particularly within the physiological pH range (6–8), facilitating its self-assembly from a swelling state to a phase-separation state.

The surface charge differences between Prot-GA and Prot-CA deposited on PDMS substrates were also directly investigated by  $\Delta I$ -SICM in diluted saline (Figure 3A), with a negatively charged BSA coating serving as the control group. The equivalent circuit diagram in Figure 3B illustrates the overall distance-dependent variation of the ion current.<sup>32</sup> In this work, the ARS and skip dual modes were implemented to enable precise scanning and avoid lateral interference between the scanning probe and the scanned cell membrane surfaces, as previously reported. During fine scanning, the nanopipette was brought closer to the substrate from an initial position ( $D_{\text{ps-max}}$ ) and halted at  $D_{\text{ps-min}}$  once the current decreased to the set threshold. Subsequently, the nanopipette was retracted from  $D_{\text{ps-min}}$  back to  $D_{\text{ps-max}}$ . The current difference ( $\Delta I$ , the

absolute difference between  $I_{\text{ps-max}}$  and  $I_{\text{ps-min}}$ ) was correlated to the surface charge density, with a higher value indicating a more negatively charged surface (Figure 3C). The topographical and  $\Delta I$  images of BSA, Prot-GA, and Prot-CA coatings (0.5  $\text{mg/mL}$ ) are shown in Figure 3D–F. Compared to the  $\Delta I$  recorded on the BSA coating (Figure 3D), significant decreases in  $\Delta I$  were observed for both Prot-GA (Figure 3E) and Prot-CA (Figure 3F) coatings, suggesting the shifting of surface charge from negative to positive values for Prot-GA and Prot-CA coatings due to their positively charged guanidyl groups. Meanwhile, the  $\Delta I$  on the Prot-GA coating was relatively smaller than that on the Prot-CA coating, which was consistent with the zeta potential measurement (Figure S6). In summary, Prot-CA tends to assemble into relatively smaller structures compared to Prot-GA at the same mass concentration, which might be ascribed to the chemical functionalities of adjacent catecholamine structures and the respective surface charges.<sup>33</sup> Protein-based Prot-CA coacervates with a nanosized diameter and a relatively controllable phase separation process are more appropriate to be engineered as the nanovesicles.

**Interaction between Prot-CA and Lipid Layers.** The interaction between the Prot-based vesicles and lipids was directly measured by a bubble probe surface force technique by AFM (MFP-3D, Oxford Instrument).<sup>34–36</sup> Figure 4A illustrates a schematic of the liquid bubble-surface AFM force measurement experiment alongside the microscopic image of a typical bubble-anchored AFM probe and the topographical image of a lipid-coated silicon wafer (Figure 4B). The interaction force between bubbles containing 200 ppm of

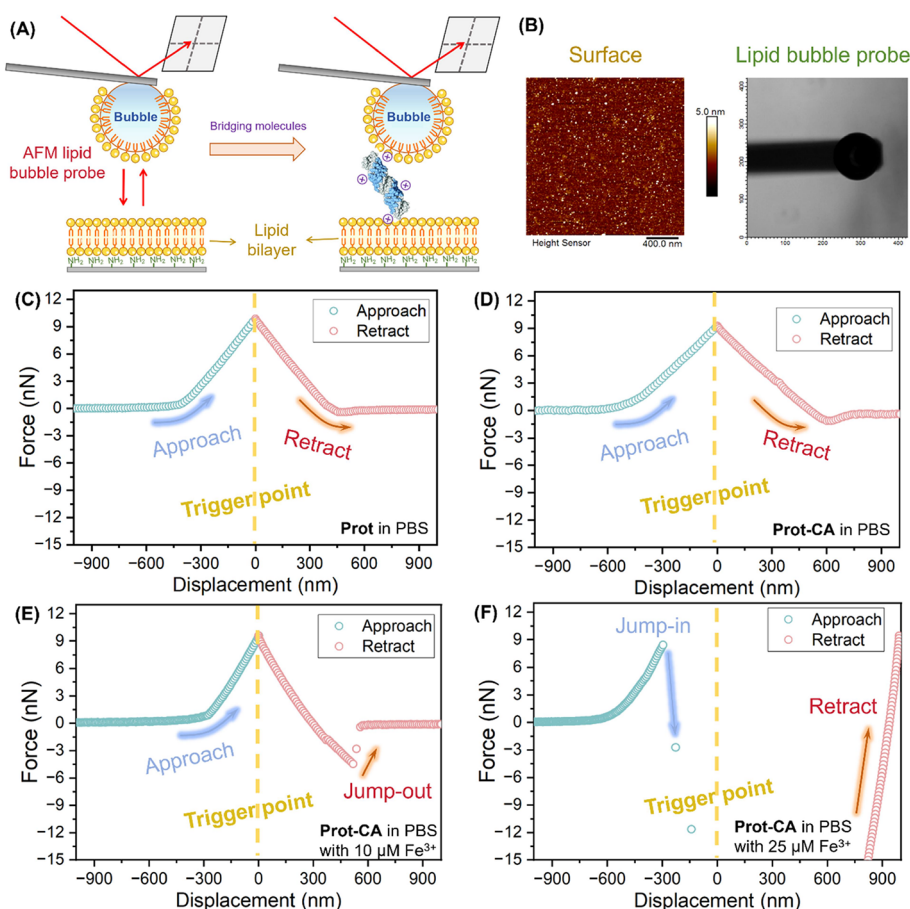


**Figure 4.** (A) Schematic representation of a typical bubble-surface AFM force measurement utilizing the bubble probe AFM technique. (B) Topological image of lipid surfaces and a microscopic image of the bubble-anchored probe. Experimentally measured interaction force profiles for a bubble stabilized with 200 ppm of DOPE and a DOPE coating with 500 ppm of (C) Prot, (D) Prot-CA, (E) Prot-CA-Fe<sup>3+</sup> (10 μM), and (F) Prot-CA-Fe<sup>3+</sup> (25 μM) in PBS.

DOPE lipid and a DOPE-coated silicon wafer in the PBS solution containing Prot and Prot-CA was determined. A lipid bubble was applied in this work to simulate the mobile but thermodynamically stable lipid layer belonging to cell membranes. The interaction force measured in pure PBS is depicted in Figure S7 as a control. Compared to the force in pure PBS, no significant change was observed with the addition of 500 ppm of Prot (Figure 4C) and Prot-CA (Figure 4D) during the approach and retraction process of the bubble probe. However, it was noted that the adhesion during the retraction of Prot-CA was slightly enhanced compared to that of Prot. To further explore the interaction, a trace amount of Fe<sup>3+</sup> was added to the solution to facilitate the binding effect between catechol groups and phosphate groups via coordination chemistry.<sup>37–39</sup> An enlarged “jump-out” behavior, approximately 5 nN, was detected during the retraction process in the PBS solution containing 500 ppm of Prot-CA and 10 μM Fe<sup>3+</sup> (Figure 4E), implying the bridging effect of Prot-CA-Fe<sup>3+</sup> (10 μM) between the lipid layers. Upon an increase in the Fe<sup>3+</sup> concentration to 25 μM Fe<sup>3+</sup> (Figure 4F), the interaction forces exhibited a notable change. A sudden “jump-in” behavior was detected after overcoming the electrostatic and hydrodynamic repulsion of approximately 8.5 nN during the approach of the DOPE bubble toward the DOPE surface, which indicated a strong interaction of Prot-CA-Fe<sup>3+</sup> (25 μM) with the lipid surfaces. Considering that the electrostatic interaction is suppressed (Debye length < 2 nm) in

PBS saline, the long-range attraction is mainly due to the bridging effect of Fe<sup>3+</sup>-chelation, which is consistent with the variation of the hydrodynamic diameter of Prot-CA (DLS analysis, Figure S5) in the presence of Fe<sup>3+</sup>.<sup>38,39</sup> The above results demonstrated that interaction forces between the lipid layers could be effectively modulated by Prot-CA in the presence of a trace amount of Fe<sup>3+</sup>, as possibly tuned by the synergistic bridging effect via coordination bonds and electrostatic interactions.<sup>40</sup>

**Interaction between Prot-CA and Gingival Fibroblasts.** With the insights of Prot-CA interacting with single lipid layers in a lipid-stabilized bubble model, the functions of Prot-CA toward cell membranes were further investigated using the  $\Delta I$ -SICM technique.<sup>41–43</sup> As illustrated in Figure 5A, we utilized  $\Delta I$ -SICM for the high-resolution imaging of the cellular membrane in situ, comparing both untreated and treated dental fibroblasts. Figure 5B indicates the topographical data of the cytoskeleton in the HGF cell, scanned over a relatively large area, revealing a well-organized and defined structure. The section of the untreated cell exhibited a reasonable structure, with heights reaching up to 6 μm. Time traces of the displacement and ionic current in coarse and fine scanning, marked by a red line in Figure 5B, are presented in Figure 5C. Figure 5D displays the topographical and corresponding  $\Delta I$  images of live HGF cells incubated with Prot-CA, Prot-CA-Fe<sup>3+</sup> (10 μM), and Prot-CA-Fe<sup>3+</sup> (25 μM), highlighting distinct cellular responses. The nanopipette



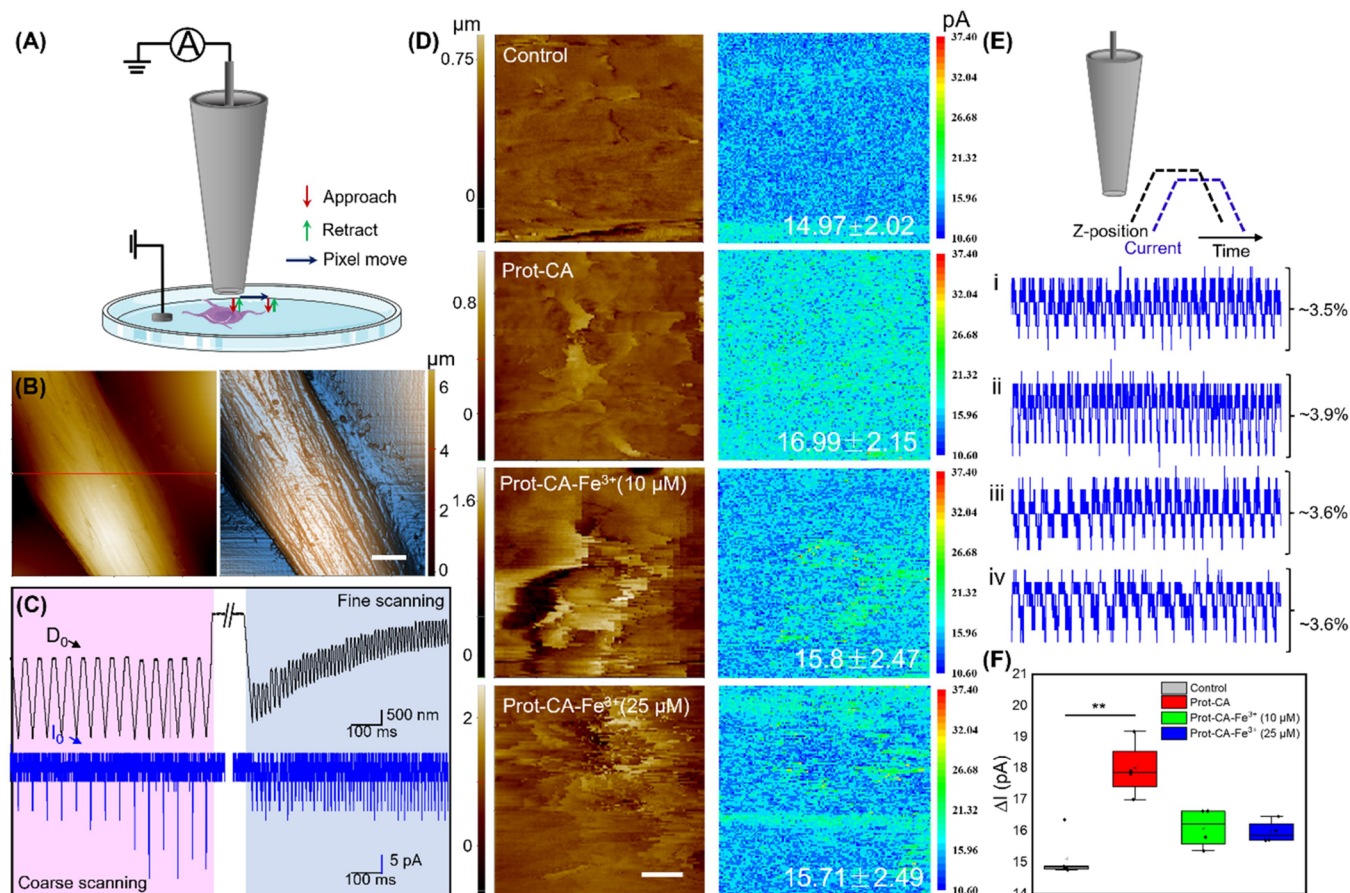


**Figure 5.** Simultaneous topographical mapping and surface charge imaging using  $\Delta I$ -based SICM. (A) Schematic representation of the  $\Delta I$ -SICM configuration for cellular imaging. (B) 2D and enhanced color topographical images of a single HGF cell. (C) Time traces of Z movement (black) and ionic current (blue) as marked in (B). (D) Simultaneous topography and  $\Delta I$  images under control and Prot-CA, Prot-CA-Fe<sup>3+</sup>(10  $\mu$ M), and Prot-CA-Fe<sup>3+</sup>(25  $\mu$ M) treatment conditions (scale bar: 1  $\mu$ m). (E) Percentage decreases in current for the control (i), Prot-CA (ii), Prot-CA-Fe<sup>3+</sup>(10  $\mu$ M) (iii), and Prot-CA-Fe<sup>3+</sup>(25  $\mu$ M) (iv) treatments. (F) Bar graphs illustrating the average  $\Delta I$  values obtained from (E).

approached the Prot-CA treated cells until a current drop of approximately 3.9% was observed, resulting in a significantly larger  $\Delta I$  compared to untreated cells. Notably, the  $\Delta I$  values for Prot-CA-treated cells were slightly more negative than those of control cells, indicating sensitivity to surface charge changes due to increased cell membrane permeability induced by the positively charged Prot-CA. In the groups of Prot-CA-Fe<sup>3+</sup>(10  $\mu$ M)- and Prot-CA-Fe<sup>3+</sup>(25  $\mu$ M)-treated cells, the nanopipette was advanced until current reductions of about 3.6% were achieved, as illustrated in Figure 5E. Lower surface charge variations and higher morphological changes of cell membranes were detected in these cells, indicative of possible local membrane disruption (Figure 5F). Considering the higher adhesion of Prot-CA-Fe<sup>3+</sup>(10  $\mu$ M) and Prot-CA-Fe<sup>3+</sup>(25  $\mu$ M) to lipid layers, the binding of Prot-CA-Fe<sup>3+</sup> to the cell membrane might dominate the interfacial interactions instead of the surface-charge-induced endocytosis of Prot-CA.

**Microbial Inhibition Performance of Prot-CA.** The antimicrobial properties of the developed Prot-CA were evaluated through a microbial growth inhibition assay, employing Gram-negative *E. coli* and Gram-positive *S. aureus*. In a typical experiment, both PAM and P(AM-Hb3/CM0.5) hydrogels were immersed in *E. coli* and *S. aureus* suspension ( $10^6$ ) and gently shaken for 4 h at room temperature. The suspension was then transferred and spread on LB agar plates, followed by an additional incubation for 12 h. The number of

*E. coli* and *S. aureus* colonies on the agar plates treated with Prot-CA, Prot-CA-Fe<sup>3+</sup>(10  $\mu$ M), and Prot-CA-Fe<sup>3+</sup>(25  $\mu$ M) is presented in Figure 6A. The colonies were counted using ImageJ for the calculation of the survival rate % after treatment compared to the control groups. As shown in Figure 6B, the antibacterial rate of Prot-CA was 72.5% against *E. coli* and 62.4% against *S. aureus*. After introducing a trace amount of Fe<sup>3+</sup> at concentrations of 10 and 25  $\mu$ M (within the serum iron content range of healthy humans), the antibacterial rates of Prot-CA-Fe<sup>3+</sup>(10  $\mu$ M) and Prot-CA-Fe<sup>3+</sup>(25  $\mu$ M) were elevated significantly to over 98% for *E. coli* and over 99% for *S. aureus*.<sup>44,45</sup> A proposed bacterial inhibition mechanism of Prot-CA and Prot-CA-Fe<sup>3+</sup> is illustrated in Figure 6C, wherein positively charged guanidyl groups and Fe<sup>3+</sup>-chelation synergistically facilitated the bonding of nanovesicles to the bacterial membrane, intermediating the membrane function and reducing microbial growth.<sup>46–48</sup> As the cargo molecules for drug encapsulation/release, the native antimicrobial functions of Prot-CA demonstrate its great potential in providing multifunctional yet antibiotic-free in situ treatment of pathological tissues, such as infected wounds.

## CONCLUSIONS

In conclusion, we demonstrated the design of a new class of Prot-based nonphospholipid nanovesicles, of which a spontaneous phase separation was observed in the alkaline environ-



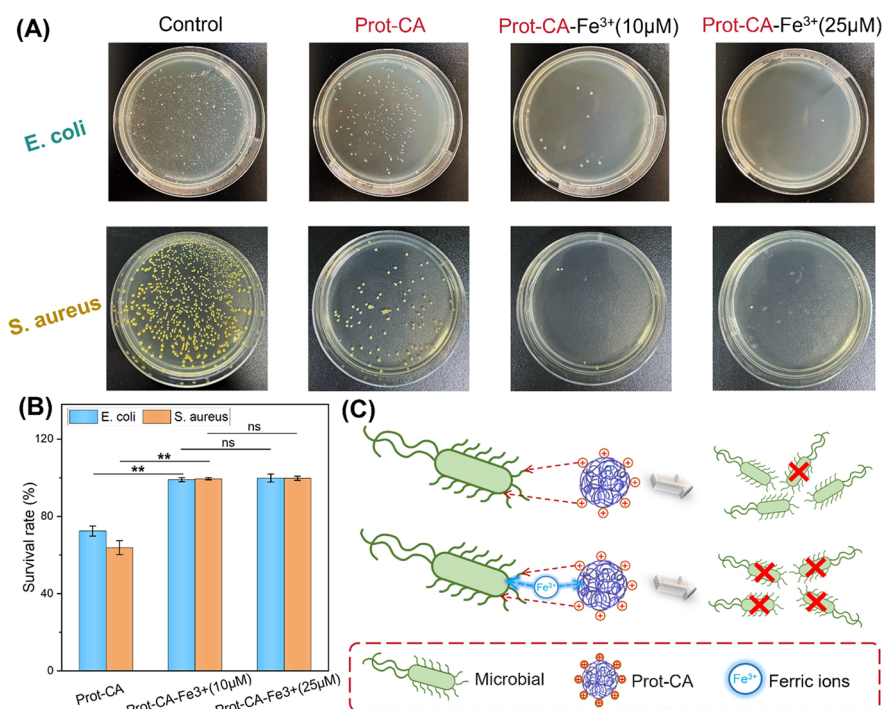


**Figure 6.** Analysis of the antibacterial properties exhibited by the nanovesicles. (A) The antibacterial rate of *E. coli* and *S. aureus* colonies for the control group, Prot-CA group, Prot-CA-Fe<sup>3+</sup> (10 μM) group, and Prot-CA-Fe<sup>3+</sup> (25 μM) group ( $\pm$ SD for  $n \geq 3$  replicates per condition,  $p < 0.01$  and  $> 0.05$ ). (B) Quantitative analysis of colonies after treatment with Prot-CA, Prot-CA-Fe<sup>3+</sup> (10 μM), and Prot-CA-Fe<sup>3+</sup> (25 μM). (C) Proposed synergistic antibacterial mechanisms.

ment by grafting CA and GA groups to the Prot. Compared to Prot-GA, which assembled into a microscopic structure ( $>1$  μm), Prot-CA assembled into a relatively smaller structure ( $\sim 200$  nm), which was not suitable for the development of nanovesicles. Lipid bubble force measurements were performed to investigate the nanomechanical mechanisms between the developed Prot-CA and single-layer lipids immobilized at the air–water interface. It was found that grafting CA onto Prot effectively enhanced their adhesion to lipid layers, while the apparent bridging effect (strong adhesion) was measured between Prot-CA and lipids by further introducing a trace amount of Fe<sup>3+</sup> (up to 25 μM). The bonding affinity to the lipid interfaces followed the order Prot-CA > Prot-GA > original Prot. Moreover, the interaction of Prot-CA with the living HGF cells was investigated by SICM. An increase in surface charge on cell membranes (indicated by elevated  $\Delta I$ ) was observed, indicating the effect of Prot-CA in enhancing the cell permeability. Introducing a trace amount of Fe<sup>3+</sup> could further adjust the functionality of Prot-CA via the bridging effect-induced lipid-binding capability. The function of Prot-CA in bacterial membranes was also demonstrated by a microbial growth inhibition assay. Prot-GA successfully inhibited the growth of both Gram-negative *E. coli* (antibacterial rate  $> 98\%$ ) and Gram-positive *S. aureus* (antibacterial rate  $> 99\%$ ) with the assistance of 10 μM Fe<sup>3+</sup>. Hence, the attachment behavior of Prot to cell membrane-like lipid layers could be enhanced by the grafting of CA and further adjusted by the Fe<sup>3+</sup> concentration, potentially modulating their penetration behavior toward lipid membranes. This work improves the fundamental understanding of the surface interaction mechanisms between cationic proteins and lipid-based biological barriers, which is beneficial for

enhancing therapeutic outcomes of protein-based nonphospholipid nanovesicles in the future.

## ■ ASSOCIATED CONTENT

### Supporting Information

The Supporting Information is available free of charge at <https://pubs.acs.org/doi/10.1021/acs.langmuir.4c03941>.

XPS N 1s of the samples (Figure S1), SEM images (Figure S2) and fluorescent images (Figure S3) of the samples, entrapment efficiency of Prot-CA (Figure S4), zeta potentials of the samples (Figure S5), force profiles (Figure S6), and DLS (Figure S7) analysis of the samples (PDF)

## ■ AUTHOR INFORMATION

### Corresponding Authors

**Qing Pan** – Department of Stomatology, The Second People's Hospital of Changzhou, The Third Affiliated Hospital of Nanjing Medical University, Changzhou Medical Center, Nanjing Medical University, Changzhou 213164, China; Email: [qing\\_pan@outlook.com](mailto:qing_pan@outlook.com)

**Feng Chen** – Key Laboratory for Bio-Electromagnetic Environment and Advanced Medical Theranostics, School of Biomedical Engineering and Informatics, Nanjing Medical University, Nanjing 211166, China; Email: [chenfeng@njmu.edu.cn](mailto:chenfeng@njmu.edu.cn)

**Bin Yan** – National Engineering Laboratory for Clean Technology of Leather Manufacture, College of Biomass Science and Engineering, Sichuan University, Chengdu 610065, China; [orcid.org/0000-0001-5426-6179](https://orcid.org/0000-0001-5426-6179); Email: [binyan@scu.edu.cn](mailto:binyan@scu.edu.cn)

## Authors

**Haibing Yang** — Department of Stomatology, The Second People's Hospital of Changzhou, The Third Affiliated Hospital of Nanjing Medical University, Changzhou Medical Center, Nanjing Medical University, Changzhou 213164, China

**Yao Song** — Key Laboratory for Bio-Electromagnetic Environment and Advanced Medical Theranostics, School of Biomedical Engineering and Informatics, Nanjing Medical University, Nanjing 211166, China

**Qiang Zhang** — Key Laboratory for Bio-Electromagnetic Environment and Advanced Medical Theranostics, School of Biomedical Engineering and Informatics, Nanjing Medical University, Nanjing 211166, China

**Moran Wang** — Key Laboratory for Bio-Electromagnetic Environment and Advanced Medical Theranostics, School of Biomedical Engineering and Informatics, Nanjing Medical University, Nanjing 211166, China

**Tianqi Jia** — Key Laboratory for Bio-Electromagnetic Environment and Advanced Medical Theranostics, School of Biomedical Engineering and Informatics, Nanjing Medical University, Nanjing 211166, China

**Kanda Sun** — Department of Stomatology, The Second People's Hospital of Changzhou, The Third Affiliated Hospital of Nanjing Medical University, Changzhou Medical Center, Nanjing Medical University, Changzhou 213164, China

**Xiang Guan** — Key Laboratory for Bio-Electromagnetic Environment and Advanced Medical Theranostics, School of Biomedical Engineering and Informatics, Nanjing Medical University, Nanjing 211166, China

**Mingfei Pan** — Department of Stomatology, The Second People's Hospital of Changzhou, The Third Affiliated Hospital of Nanjing Medical University, Changzhou Medical Center, Nanjing Medical University, Changzhou 213164, China; Key Laboratory for Bio-Electromagnetic Environment and Advanced Medical Theranostics, School of Biomedical Engineering and Informatics, Nanjing Medical University, Nanjing 211166, China; [orcid.org/0000-0001-8436-2671](https://orcid.org/0000-0001-8436-2671)

Complete contact information is available at:

<https://pubs.acs.org/10.1021/acs.langmuir.4c03941>

## Author Contributions

<sup>†</sup>H.Y. and Y.S. have contributed equally to the study.

## Author Contributions

This manuscript was written through the contributions of all authors. All authors have approved to the final version of the manuscript.

## Notes

The authors declare no competing financial interest.

## ACKNOWLEDGMENTS

The authors are grateful for the financial support from the Basic Research Project of Changzhou Medical Center of Nanjing Medical University (CMCB202317), the Outstanding Postdoctoral Fellow of Jiangsu Province (M.P. and X.G.), and the Science and Technology Development Fund of Nanjing Medical University—General Project (NMUB20230047).

## REFERENCES

- (1) Grimaldi, N.; Andrade, F.; Segovia, N.; Ferrer-Tasies, L.; Sala, S.; Veciana, J.; Ventosa, N. Lipid-based nanovesicles for nanomedicine. *Chem. Soc. Rev.* **2016**, *45* (23), 6520–6545.
- (2) Wadhwa, S.; Garg, V.; Gulati, M.; Kapoor, B.; Singh, S. K.; Mittal, N. Nanovesicles for nanomedicine: theory and practices. *Pharmaceutical Nanotechnology: Basic Protocols* **2019**, 2000, 1–17.
- (3) Xu, H.; Lu, J.; Xi, Y.; Wang, X.; Liu, J. Liquid metal biomaterials: translational medicines, challenges and perspectives. *Natl. Sci. Rev.* **2024**, *11* (2), No. nwad302.
- (4) Olsén, E.; Jõemetsa, S.; González, A.; Joyce, P.; Zhdanov, V. P.; Midtvedt, D.; Hook, F. Diffusion of lipid nanovesicles bound to a lipid membrane is associated with the partial-slip boundary condition. *Nano Lett.* **2021**, *21* (19), 8503–8509.
- (5) Guo, Y.; Cao, X.; Zheng, X.; Abbas, S. J.; Li, J.; Tan, W. Construction of nanocarriers based on nucleic acids and their applications in nanobiology delivery systems. *Natl. Sci. Rev.* **2022**, *9* (5), No. nwac006.
- (6) Lee, J.; Noh, M.; Jang, J.; Lee, J. B.; Hwang, Y.-H.; Lee, H. Skin penetration enhancer-incorporated lipid nanovesicles (SPE-LNV) for skin brightening and wrinkle treatment. *ACS Appl. Mater. Interfaces* **2022**, *14* (32), 36331–36340.
- (7) Jang, S. C.; Kim, O. Y.; Yoon, C. M.; Choi, D.-S.; Roh, T.-Y.; Park, J.; Nilsson, J.; Lotvall, J.; Kim, Y.-K.; Gho, Y. S. Bioinspired exosome-mimetic nanovesicles for targeted delivery of chemotherapeutics to malignant tumors. *ACS Nano* **2013**, *7* (9), 7698–7710.
- (8) Peruzzi, J. A.; Gunnels, T. F.; Edelstein, H. I.; Lu, P.; Baker, D.; Leonard, J. N.; Kamat, N. P. Enhancing extracellular vesicle cargo loading and functional delivery by engineering protein-lipid interactions. *Nat. Commun.* **2024**, *15* (1), 5618.
- (9) Yan, B.; He, C.; Chen, S.; Xiang, L.; Gong, L.; Gu, Y.; Zeng, H. Nanoconfining cation- $\pi$  interactions as a modular strategy to construct injectable self-healing hydrogel. *CCS Chemistry* **2022**, *4* (8), 2724–2737.
- (10) Ren, Y.; Nie, L.; Zhu, S.; Zhang, X. Nanovesicles-mediated drug delivery for oral bioavailability enhancement. *Int. J. Nanomed.* **2022**, *17*, 4861.
- (11) Xu, Y.; Lv, J.; Kong, C.; Liu, Y.; Wang, K.; Tang, Z.; Chen, X. Introducing urea into tirapazamine derivatives to enhance anticancer therapy. *Natl. Sci. Rev.* **2024**, *11* (4), No. nwae038.
- (12) Omura, M.; Morimoto, K.; Araki, Y.; Hirose, H.; Kawaguchi, Y.; Kitayama, Y.; Goto, Y.; Harada, A.; Fujii, I.; Takatani-Nakase, T. Inkjet-Based Intracellular Delivery System that Effectively Utilizes Cell-Penetrating Peptides for Cytosolic Introduction of Biomacromolecules through the Cell Membrane. *ACS Appl. Mater. Interfaces* **2023**, *15* (41), 47855–47865.
- (13) Zhang, X.; Malle, M. G.; Thomsen, R. P.; Sørensen, R. S.; Sørensen, E. W.; Hatzakis, N. S.; Kjems, J. Deconvoluting the Effect of Cell-Penetrating Peptides for Enhanced and Controlled Insertion of Large-Scale DNA Nanopores. *ACS Appl. Mater. Interfaces* **2024**, *16* (15), 18422–18433.
- (14) Derakhshankhah, H.; Jafari, S. Cell penetrating peptides: A concise review with emphasis on biomedical applications. *Biomed. Pharmacother.* **2018**, *108*, 1090–1096.
- (15) Xia, H.; Gao, X.; Gu, G.; Liu, Z.; Zeng, N.; Hu, Q.; Song, Q.; Yao, L.; Pang, Z.; Jiang, X. Low molecular weight protamine-functionalized nanoparticles for drug delivery to the brain after intranasal administration. *Biomaterials* **2011**, *32* (36), 9888–9898.
- (16) Ruseska, I.; Fresacher, K.; Petschacher, C.; Zimmer, A. Use of protamine in nanopharmaceuticals—A review. *Nanomaterials* **2021**, *11* (6), 1508.
- (17) Moritz, L.; Schon, S. B.; Rabbani, M.; Sheng, Y.; Agrawal, R.; Glass-Klaiber, J.; Sultan, C.; Camarillo, J. M.; Clements, J.; Baldwin, M. R. Sperm chromatin structure and reproductive fitness are altered by substitution of a single amino acid in mouse protamine 1. *Nat. Struct. Mol. Biol.* **2023**, *30* (8), 1077–1091.
- (18) Ahn, B. K.; Das, S.; Linstadt, R.; Kaufman, Y.; Martinez-Rodriguez, N. R.; Mirshafian, R.; Kesselman, E.; Talmon, Y.; Lipshutz,

- B. H.; Israelachvili, J. N. High-performance mussel-inspired adhesives of reduced complexity. *Nat. Commun.* **2015**, *6* (1), 8663.
- (19) Rapp, M. V.; Maier, G. P.; Dobbs, H. A.; Higdon, N. J.; Waite, J. H.; Butler, A.; Israelachvili, J. N. Defining the catechol–cation synergy for enhanced wet adhesion to mineral surfaces. *J. Am. Chem. Soc.* **2016**, *138* (29), 9013–9016.
- (20) Xie, L.; Shi, C.; Cui, X.; Huang, J.; Wang, J.; Liu, Q.; Zeng, H. Probing the interaction mechanism between air bubbles and bitumen surfaces in aqueous media using bubble probe atomic force microscopy. *Langmuir* **2018**, *34* (3), 729–738.
- (21) Lu, Q.; Oh, D. X.; Lee, Y.; Jho, Y.; Hwang, D. S.; Zeng, H. Nanomechanics of cation– $\pi$  interactions in aqueous solution. *Angew. Chem.* **2013**, *125* (14), 4036–4040.
- (22) Geng, H.; Zhang, P.; Peng, Q.; Cui, J.; Hao, J.; Zeng, H. Principles of cation– $\pi$  interactions for engineering mussel-inspired functional materials. *Acc. Chem. Res.* **2022**, *55* (8), 1171–1182.
- (23) Pan, M.; Wu, M.; Shui, T.; Xiang, L.; Yang, W.; Wang, W.; Liu, X.; Wang, J.; Chen, X.-Z.; Zeng, H. Highly stretchable, elastic, antimicrobial conductive hydrogels with environment-adaptive adhesive property for health monitoring. *J. Colloid Interface Sci.* **2022**, *622*, 612–624.
- (24) Pan, M.; Shui, T.; Zhao, Z.; Li, M.; Fan, H.; Wu, J.; Zeng, H. Orchestrating Asymmetric Surface Functionalities on Hydrogel Stamps where Adhesion Meets Lubrication. *Chem. Mater.* **2023**, *35* (13), 4998–5008.
- (25) Kim, S.; Huang, J.; Lee, Y.; Dutta, S.; Yoo, H. Y.; Jung, Y. M.; Jho, Y.; Zeng, H.; Hwang, D. S. Complexation and coacervation of like-charged polyelectrolytes inspired by mussels. *Proc. Natl. Acad. Sci. U. S. A.* **2016**, *113* (7), E847–E853.
- (26) Hong, Y.; Najafi, S.; Casey, T.; Shea, J.-E.; Han, S.-I.; Hwang, D. S. Hydrophobicity of arginine leads to reentrant liquid-liquid phase separation behaviors of arginine-rich proteins. *Nat. Commun.* **2022**, *13* (1), 7326.
- (27) Albarran, G.; Boggess, W.; Rassolov, V.; Schuler, R. H. Absorption spectrum, mass spectrometric properties, and electronic structure of 1, 2-benzoquinone. *J. Phys. Chem. A* **2010**, *114* (28), 7470–7478.
- (28) Catauro, M.; Barrino, F.; Dal Poggetto, G.; Crescente, G.; Piccolella, S.; Pacifico, S. New SiO<sub>2</sub>/caffeic acid hybrid materials: Synthesis, spectroscopic characterization, and bioactivity. *Materials* **2020**, *13* (2), 394.
- (29) Kurt, A. H.; Olutas, E. B.; Avcioglu, F.; Karakuş, H.; Sungur, M. A.; Oztabag, C. K.; Yıldırım, M. Quercetin-and caffeic acid-functionalized chitosan-capped colloidal silver nanoparticles: one-pot synthesis, characterization, and anticancer and antibacterial activities. *Beilstein J. Nanotechnol.* **2023**, *14* (1), 362–376.
- (30) Permatasari, F. A.; Aimon, A. H.; Iskandar, F.; Ogi, T.; Okuyama, K. Role of C–N configurations in the photoluminescence of graphene quantum dots synthesized by a hydrothermal route. *Sci. Rep.* **2016**, *6*, No. 21042.
- (31) Almeida, L. C.; Frade, T.; Correia, R. D.; Niu, Y.; Jin, G.; Correia, J. P.; Viana, A. S. Electrosynthesis of polydopamine-ethanolamine films for the development of immunosensing interfaces. *Sci. Rep.* **2021**, *11* (1), 2237.
- (32) Chen, F.; Panday, N.; Li, X.; Ma, T.; Guo, J.; Wang, X.; Kos, L.; Hu, K.; Gu, N.; He, J. Simultaneous mapping of nanoscale topography and surface potential of charged surfaces by scanning ion conductance microscopy. *Nanoscale* **2020**, *12* (40), 20737–20748.
- (33) Fan, H.; Wang, J.; Tao, Z.; Huang, J.; Rao, P.; Kurokawa, T.; Gong, J. P. Adjacent cationic–aromatic sequences yield strong electrostatic adhesion of hydrogels in seawater. *Nat. Commun.* **2019**, *10* (1), 5127.
- (34) Qiao, C.; Yang, D.; Mao, X.; Xie, L.; Gong, L.; Peng, X.; Peng, Q.; Wang, T.; Zhang, H.; Zeng, H. Recent advances in bubble-based technologies: Underlying interaction mechanisms and applications. *Appl. Phys. Rev.* **2021**, *8*, No. 011315.
- (35) Cui, X.; Liu, J.; Xie, L.; Huang, J.; Liu, Q.; Israelachvili, J. N.; Zeng, H. Modulation of hydrophobic interaction by mediating surface nanoscale structure and chemistry, not monotonically by hydrophobicity. *Angew. Chem.* **2018**, *130* (37), 12079–12084.
- (36) Pan, M.; Gong, L.; Xiang, L.; Yang, W.; Wang, W.; Zhang, L.; Hu, W.; Han, L.; Zeng, H. Modulating surface interactions for regenerable separation of oil-in-water emulsions. *J. Membr. Sci.* **2021**, *625*, No. 119140.
- (37) Mesko, M.; Xiang, L.; Bohle, S.; Hwang, D. S.; Zeng, H.; Harrington, M. J. Catechol-vanadium binding enhances cross-linking and mechanics of a mussel byssus coating protein. *Chem. Mater.* **2021**, *33* (16), 6530–6540.
- (38) Yang, W.; Pan, M.; Zhang, J.; Zhang, L.; Lin, F.; Liu, X.; Huang, C.; Chen, X. Z.; Wang, J.; Yan, B.; Zeng, H. A universal strategy for constructing robust and antifouling cellulose nanocrystal coating. *Adv. Funct. Mater.* **2022**, *32* (8), No. 2109989.
- (39) Pan, M.; Nguyen, K.-C. T.; Yang, W.; Liu, X.; Chen, X.-Z.; Major, P. W.; Le, L. H.; Zeng, H. Soft armour-like layer-protected hydrogels for wet tissue adhesion and biological imaging. *Chem. Eng. J.* **2022**, *434*, No. 134418.
- (40) Lu, Q.; Danner, E.; Waite, J. H.; Israelachvili, J. N.; Zeng, H.; Hwang, D. S. Adhesion of mussel foot proteins to different substrate surfaces. *J. R. Soc. Interface* **2013**, *10* (79), 20120759.
- (41) Chen, F.; He, J.; Manandhar, P.; Yang, Y.; Liu, P.; Gu, N. Gauging surface charge distribution of live cell membrane by ionic current change using scanning ion conductance microscopy. *Nano-scale* **2021**, *13* (47), 19973–19984.
- (42) Song, Y.; Zhang, S.; Cao, C.; Yan, J.; Li, M.; Li, X.; Chen, F.; Gu, N. Imaging Structural and Electrical Changes of Aging Cells Using Scanning Ion Conductance Microscopy. *Small Methods* **2024**, *8* (8), No. 2301315.
- (43) Wang, D.; Sun, L.; Okuda, S.; Yamamoto, D.; Nakayama, M.; Oshima, H.; Saito, H.; Kouyama, Y.; Mimori, K.; Ando, T. Nano-scale physical properties characteristic to metastatic intestinal cancer cells identified by high-speed scanning ion conductance microscope. *Biomaterials* **2022**, *280*, No. 121256.
- (44) Sun, H.-Q.; Lu, X.-M.; Gao, P.-J. The exploration of the antibacterial mechanism of Fe<sup>3+</sup> against bacteria. *Braz. J. Microbiol.* **2011**, *42*, 410–414.
- (45) Crosby, W. H.; Likhite, V. V.; O'Brien, J. E.; Forman, D. Serum iron levels in ostensibly normal people. *JAMA* **1974**, *227* (3), 310–312.
- (46) Fu, J.; Liu, X.; Cui, Z.; Zheng, Y.; Jiang, H.; Zhang, Y.; Li, Z.; Liang, Y.; Zhu, S.; Chu, P. K. Probiotic-based nanoparticles for targeted microbiota modulation and immune restoration in bacterial pneumonia. *Natl. Sci. Rev.* **2023**, *10* (2), No. nwac221.
- (47) Leong, M.; Parker, C. J.; Shaw, Z.; Huang, L. Z.; Nisbet, D. R.; Daeneke, T.; Elbourne, A.; Cheeseman, S. Metallic Gallium Droplets Exhibit Poor Antibacterial Properties. *ACS Appl. Mater. Interfaces* **2024**, *16* (1), 332–341.
- (48) Chen, A.; Karanastasis, A.; Casey, K. R.; Necelis, M.; Carone, B. R.; Caputo, G. A.; Palermo, E. F. Cationic molecular umbrellas as antibacterial agents with remarkable cell-type selectivity. *ACS Appl. Mater. Interfaces* **2020**, *12* (19), 21270–21282.
- (49) Kuddannaya, S.; Chuah, Y. J.; Lee, M. H. A.; Menon, N. V.; Kang, Y.; Zhang, Y. Surface chemical modification of poly (dimethylsiloxane) for the enhanced adhesion and proliferation of mesenchymal stem cells. *ACS Appl. Mater. Interfaces* **2013**, *5* (19), 9777–9784.